# Development of Body Rotation Mechanism for Wheeled Robot to Enhance Trafficability and Overcome Mobility Limitation

**KUN-JUNG KIM** [1], **BYEONG-SEOP SIM** [2], **AND KEE-HO YU** [1,3], (Senior Member, IEEE)

[1] Department of Aerospace Engineering, Jeonbuk National University, Jeonju, Jeonbuk 54896, South Korea
[2] Department of Production Engineering, UCONSYSTEM Company Ltd., Daejeon 34015, South Korea
[3] Future Air Mobility Research Center, Jeonbuk National University, Jeonju, Jeonbuk 54896, South Korea

Corresponding author: Kee-Ho Yu (yu@chonbuk.ac.kr)

**ABSTRACT** A wheeled robot operating on various complex terrains with scattered obstacles and steep slopes must be capable of surmounting obstructions and coping with the extreme driving environment. This paper proposes a body rotation mechanism that controls the load distribution on the robot wheel for the robot to surmount rocky obstacles and steadily ascend deformable slopes. This work formulates a robot dynamics model based on the wheel–complex terrain interaction model to analyze the mechanical effect of the proposed body rotation mechanism. Moreover, an optimal body rotation configuration integrating the robot dynamics model and non-dominated sorting genetic algorithm-II is obtained to choose the appropriate body rotation control strategy. The numerical analysis results conclusively prove the effectiveness of the proposed mechanism. The robot with its fabricated platform is field tested by allowing it to surmount a rocky obstacle and ascend a deformable slope. The results indicate that the proposed body rotation mechanism is an effective approach for enhancing the mobility of a wheeled robot in traversing complex terrains.

**INDEX TERMS** Trafficability, mobility limitation, body rotational wheeled robot, optimal body rotation configuration.

## I. INTRODUCTION

Sometimes, wheeled robots provide indispensable service to humans. Moreover, they are employed in the military, planetary exploration, and other fields. A robot can function as a human substitute. It can move around in configured space dictated by its mission. However, during operation, it may encounter extreme environments, such as those with steep slopes and several obstacles. As the robot surmounts an obstacle, or ascends/descends a deformable terrain, the robot may require more electric power. It may experience unequal/low traction condition, causing it to reach its torque limitation. This may be attributed to the load concentration on the driving part of the robot, causing the robot to stall or slip on a deformable complex terrain. Consequently, the robot's mobility performance, which is related to trafficability and torque limitation, may be degraded and affect mission execution.

The associate editor coordinating the review of this manuscript and approving it for publication was Jingang Jiang [ID].

Hence, for their successful operation, a robot must be capable of coping with various driving environments.

To overcome the foregoing obstructions, a number of researchers have conducted extensive studies considering the wheel–terrain interaction in relation with trafficability [1]–[4] and alternatives for improving the mobility performance of robots [5]–[10]. In addition, various locomotion mechanisms have been tried to make the robot reconfigurable [11]–[15]. In particular, the concept of a reconfigurable wheeled robot in which the center of mass may be shifted was investigated to enhance mobility performance under extreme driving conditions [3], [4], [16], [17]. The effect moving the center of mass was also analyzed [16]–[24]. Although some of the conceived alternatives can significantly improve the mobility performance, they require a complex control and transmission structure. Some concepts also require considerable energy-consuming locomotion to maintain its rotated state. To fully realize these alternatives, appropriate control strategies are necessary to define the conditions that require their implementation.

Accordingly, this paper proposes a body rotation mechanism with an appropriate body control configuration for a wheeled robot. Compared with other techniques, the proposed mechanism affords certain advantages, such as the following. It provides a higher gear ratio and torque with the least volume. Moreover, it allows irreversible force transmission for body rotation. Therefore, the mechanism does not require continuous electric power to maintain its rotated state.

The basic idea of the proposed mechanism was presented as preliminary work in a previous study of the authors [25] in which a mechanical model was developed and tested indoors on a rigid surface. However, from the realistic point of view, the mobility performance of the robot on a complex deformable terrain and the appropriate control strategy have not been well explored. Hence, this study mainly presents the mobility performance based on the wheel–complex terrain interaction. Numerical and outdoor experiments with an optimal control configuration are further conducted to verify the improvement related to mobility performance in surmounting a rocky obstacle and moving on a slope with soft-soil.

In this paper, the body rotation mechanism, which can enhance the mobility of a wheeled robot in surmounting rocky obstacles and traversing inclined deformable terrains, is presented. Mechanical and robot dynamics models based on the wheel–complex terrain interaction are also described in this work. As the model surmounts the bumpy obstacle and negotiates the inclined deformable terrain, the relationship between body rotation configuration, load distribution, trafficability, and torque limitation criterion is analyzed. In particular, the body rotation control is optimized using the formulated robot dynamics model and non-dominated sorting genetic algorithm-II (NSGA-II). Thereafter, the optimal body rotation configuration was obtained. Based on the numerical analysis results, a wheeled robot platform with a body rotation mechanism for shifting the center of mass was designed and fabricated. The effectiveness of the proposed mechanism with the optimal control configuration was fully demonstrated by field tests involving surmounting a rocky obstacle and traversing a deformable slope.

The rest of this paper is organized as follows. In the next section, the wheeled robot platform with its body rotation mechanism is described. Section III discusses the effectiveness of the proposed body rotation mechanism. In Section IV, the optimal body control configuration and numerical analysis are elaborated. Section V presents the field test results and discussion. Finally, Section VI summarizes the conclusion.

## II. ROBOT PLATFORM WITH BODY ROTATION MECHANISM

### A. STRUCTURE OF WHEELED ROBOT PLATFORM

The structure of the wheeled robot platform with the body rotation mechanism designed in this study is shown in Fig. 1; the specifications are summarized in Table 1. The robot platform is composed of the main body, parts of the rotating
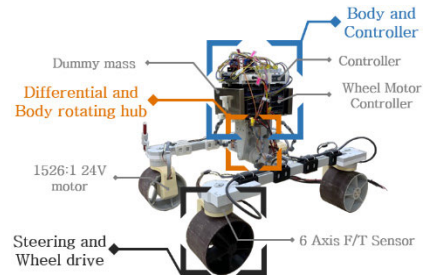


**FIGURE 1.** Wheeled robot platform configuration and components.

**TABLE 1.** Wheeled robot platform specifications.

| Description | Value |
|---|---|
| *Total robot mass* | 15.3 kg |
| *Dummy payload* | 5 kg |
| *Body rotation hub mass* | 3.3 kg |
| *Rocker link and Steering mass (one side)* | 1.47 kg |
| *Force/Torque sensor mass (each)* | 0.27 kg |
| *Wheel drive part mass (each)* | 0.7 kg |
| *Rotating body arm length* | 0.22 m |
| *Height from ground to rotation center* | 0.23 m |
| *Wheelbase* | 0.6 m |
| *Axle track* | 0.46 m |
| *Wheel radius* | 0.08 m |
| *Wheel width* | 0.12 m |

mechanism, and driving parts with simple four-wheeled struts. It is equipped with certain sensors to facilitate the collection of experimental data. A gyro-accelerometer is set at the mounting flange of the rocker link, enabling the direct measurement of the robot's inclination. A rotary potentiometer located on the mounting flange of the epicyclic gear box measures the main body's rotation angle with respect to the wheel-ground contact point. The force and torque sensors, which have six degrees of freedom, are located on the mounting flange of each steering arm to measure the generalized forces of the wheel. The encoders built into the wheel motor measure the wheel's rotational speed. To calculate the wheel torque, the current consumptions of the motor are measured. The specifications of parts are summarized in Table 2.

**TABLE 2.** Specification of robot parts.

| | |
|---|---|
| *Main controller* | NI: myRIO-1900 |
| *Gyro-accelerometer* | MPU6050 |
| *Rotary potentiometer* | RK09K11300U |
| *Force/Torque sensor* | ROBOTOUS: RFT82-HA02C |
| *Wheel driving motor* | MAXON: DCX26L GB 24V (Gear ratio 1526:1) |
| *Wheel motor controller* | MAXON: ESCON 50/5 |

### B. BODY ROTATION MECHANISM

In general, because the main components are mounted on the main body, this part accounts for most of the robot's

mass. The mounted scientific equipment and components are for power, navigation, communication, and control. Thus, rotating the robot's body is a simple and considerably effective mechanism for shifting the center of mass and load distribution.

The body rotation mechanism is designed to control the load distribution acting on each axle according to various center of mass configurations when the robot encounters and surmounts an obstacle and travels uphill or downhill a deformable terrain. The body rotation motion is shown in Fig. 2. This figure shows that the robot's body swivels from the positive to the negative direction. Then, its center of mass and normal force shift from the front to the rear wheel side, and vice versa. This process is accomplished by the epicyclical gear on the rotating hub module. The detailed structure of the proposed body rotation mechanism is shown in Fig. 3.
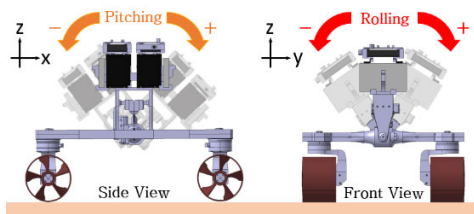


**FIGURE 2.** Concept and structure of proposed robot platform with body rotation mechanism, allowing robot to tilt and lean its main body.
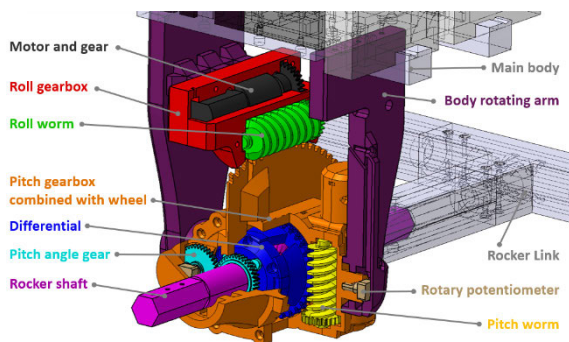


**FIGURE 3.** Structure of rotating hub module based on epicyclical gearing. Worm drive provides considerable torque with least volume for rotation; continuous power is not required to maintain rotated state.

The aforementioned figure shows the main components of the rotation hub: rocker shaft and differential, worm, idler, and sun gears. In particular, the differential gear inside the pitch gear box (the core part of the rotation hub) is connected to the rocker shaft to shift the pitch angle of the robot body. With this structure, the rocker shaft set freely rotates around the pitch angle gear, whereas the attitudes of the robot body are controlled by actuating the pitch worm joint. The worm gear with its motor connects the pitch gear box to the wheel gear to provide a wide range of robot posture according to the inclined ground angle. In particular, this mechanism not only increases the gear ratio and torque with minimal volume for

rotation but also allows the irreversible force transmission for rotating the robot body without continuous electrical power supply.

## III. EFFECTIVENESS OF BODY ROTATION MECHANISM
### A. ROBOT DYNAMICS MODEL BASED ON WHEEL–COMPLEX TERRAIN INTERACTION
#### 1) WHEEL–TERRAIN INTERACTION MODEL
In general, the trafficability of the robot on a complex terrain considerably depends on the wheel and terrain interaction. Accordingly, a wheel–terrain interaction model is employed to predict the physical phenomena that occur under the robot's wheel on the deformable terrain, as shown in Fig. 4. While traversing the deformable inclined terrain, the force and torque acting on the wheel are calculated by the integrals of the normal and shear stress under the wheel that can change the contact angle ($\theta$). Using this model, the normal stress $\sigma(\theta)$, can be represented as follows [22]:

$$\sigma(\theta) = \begin{cases} k_\sigma \left(\dfrac{r_s}{b}\right)^n (\cos\theta - \cos\theta_f)^n \\ (\theta_m \leq \theta < \theta_f) \\ k_\sigma \left(\dfrac{r_s}{b}\right)^n [\cos\left\{\theta_f - \dfrac{\theta - \theta_r}{\theta_m - \theta_r}\left(\theta_f - \theta_m\right)\right\} - \cos\theta_f]^n \\ (\theta_r < \theta \leq \theta_m), \end{cases}$$

(1)

where $r_s$ is total wheel radius; $b$ is the wheel width; $n$ is the terrain deformation exponent; and $k_\sigma$ denotes the pressure sinkage modulus. $\theta_f$, $\theta_r$ and $\theta_m$ separately represent the wheel entry angle, wheel exit angle and specific angle at which the normal stress is maximized:

$$\theta_f = \cos^{-1}(1 - \frac{z}{r_s}),$$ (2)

$$\theta_r = \cos^{-1}(1 - \frac{\kappa z}{r_s}),$$ (3)

$$\theta_m = (a_0 + a_0\lambda)\theta_f,$$ (4)

where $a_0$ and $a_1$ are specific parameter; $\kappa$ is wheel sinkage ratio; $\lambda$ denotes the slip ratio; and $z$ is sinkage, which can be geometrically obtained.
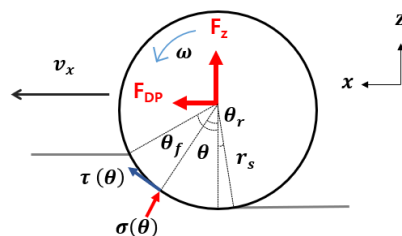


**FIGURE 4.** Stress distribution and force/torque model of wheel on deformable terrain.

Moreover, the shear stress on the driving surface, $\tau(\theta)$, which is a function of the terrain parameters and shear displacement ($j$) according to the longitudinal slip velocity ($v_{jx}$)

on the deformable terrain, is calculated as follows:

$$\tau(\theta) = (c + \sigma(\theta)\tan\varphi)[1 - e^{-j(\theta)/K}], \quad (5)$$

$$j(\theta) = \int_0^{t_0} v_{jx}\, dt = r_s[\theta_f - \theta - (1 - \lambda)(\sin\theta_f - \sin\theta)], \quad (6)$$

where $c$ is the cohesion; $\varphi$ is the internal friction angle of the terrain; $K$ denotes the fitted shear deformation modulus. The slip ratio, $\lambda$, defined as the proportion between the traveling and circumference velocities, is given as follows:

$$\lambda = \begin{cases} (r_s\omega - v_x)/(r_s\omega) & (\text{if } |r_s\omega| > |v_x|) \\ (r_s\omega - v_x)/v_x & (\text{if } |r_s\omega| < |v_x|), \end{cases} \quad (7)$$

where $v_x$ and $\omega$ are the translational and angular velocities, respectively. With this definition, the possible slip ratio values are between $-1$ and $1$.

The wheel torque ($T_w$), drawbar pull ($F_{DP}$), and normal force ($F_z$) are calculated by the integral of each stress distribution along the driving surface, as follows.

$$T_w = r_s^2 b \int_{\theta_r}^{\theta_f} \tau(\theta)\, d\theta, \quad (8)$$

$$F_{DP} = r_s b \int_{\theta_r}^{\theta_f} \{\tau(\theta)\cos\theta - \sigma(\theta)\sin\theta\}\, d\theta, \quad (9)$$

$$F_z = r_s b \int_{\theta_r}^{\theta_f} \{\tau(\theta)\sin\theta + \sigma(\theta)\cos\theta\}\, d\theta. \quad (10)$$

The analytical integration of the integrals in (8)–(10) can be exigent. It requires the reconstruction of the formula and error to express them in terms of the integrals. Thus, the composite Simpson's rule, which approximates the integral terms to reduce the identification time for each computational cycle, is applied. The process is as follows: for an arbitrary integral, $\int_a^b f(x)\, dx$, choose an even integer, $n_s$; divide $[a, b]$ into $n_s/2$ equal subintervals; and apply Simpson's rule to each interval, $[x_{2k-2}, x_{2k}]$, for $1 \le k \le n_s/2$. The approximation is given by the following [26]:

$$\int_a^b f(x)\, dx$$
$$\doteq \frac{(b-a)}{3n_s} \sum_{k=1}^{n_s/2} [f(x_{2k-2}) + 4f(x_{2k-1}) + f(x_{2k})],$$
$$\doteq \frac{(b-a)}{3n_s} [f(a) + f(b) + 2\sum_{k=1}^{n_s/2-1} f(x_{2k}) + 4\sum_{k=1}^{n_s/2} f(x_{2k-1})]. \quad (11)$$

### 2) ROBOT DYNAMICS MODEL BASED ON WHEEL–COMPLEX TERRAIN INTERACTION

The analytical model of multi-body dynamics based on the wheel–complex terrain interaction phenomena was developed to deal with the motion behavior of the body and
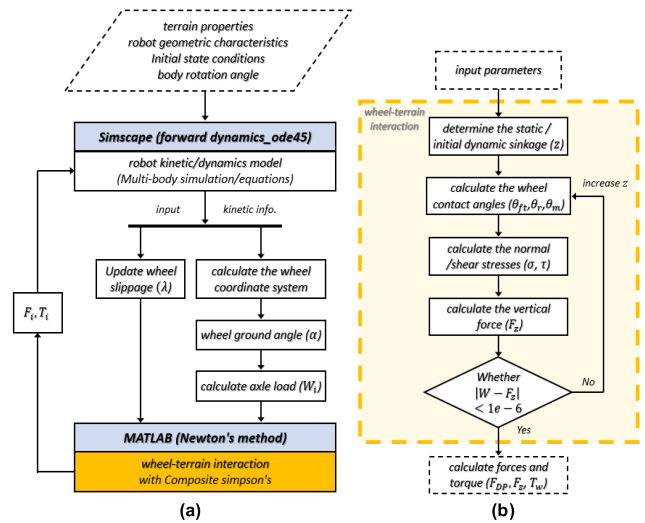


**FIGURE 5.** Overall simulation architecture for (a) wheel-robot dynamics model and (b) wheel-terrain interaction modeling.

robot wheel surmounting an obstacle and traversing an inclined deformable terrain, as shown in Fig. 5. The overall multi–body dynamics simulation architecture is composed of three major steps, as summarized in Table 3. First, using the wheel–terrain interaction model, the forces and torque on each wheel corresponding to the kinematic parameters (e.g., mass, body rotation angle, wheel parameters, and derived slip ratio state) of the rover, are calculated via a MATLAB function for Newton's method. The external forces and torque coincide with the longitudinal direction through coordinate system transformations according to the normal direction of the inclined terrain. To obtain the forward dynamic solution of (12), such as the position, orientation, and velocity of the robot, the robot dynamic model is then solved using MATLAB/ SIMULINK:

$$\begin{bmatrix} H_0 & H_{0m1} & \cdots & H_{0mk} \\ H_{0m1}^T & H_{m11} & \cdots & H_{m1k} \\ \vdots & \vdots & \ddots & \vdots \\ H_{0mk}^T & H_{m1k}^T & \cdots & H_{mkk} \end{bmatrix} \begin{bmatrix} \ddot{x}_0 \\ \dot{\varphi}_1 \\ \vdots \\ \ddot{\varphi}_k \end{bmatrix} + C + G$$
$$= \begin{bmatrix} F_0^T \\ \tau_1 \\ \vdots \\ \tau_n \end{bmatrix} + \begin{bmatrix} J_0^T F_{ex} \\ J_{m1}^T F_{ex1} \\ \vdots \\ J_{mk}^T F_{exk} \end{bmatrix}, \quad (12)$$

where $k$ is number of limbs; $H_{0,0m1,\cdots,mkk}$ denote inertia matrices for the entire system composed by the inertia property of each body; $x_0$ ($x_0 \in \mathbf{R}^6$) is position/orientation of the base body; $\varphi\{(\varphi_1^T, \cdots, \varphi_k^T)^T \in \mathbf{R}^n\}$ is articulated joint angles; $C$ is non-linear velocity-dependent term; $G$ is gravity term; $F_0$ $\{F_0 \in \mathbf{R}^6\}$ is forces/moment exerted on the base body; $\tau\{(\tau_1^T, \cdots, \tau_k^T)^T \in \mathbf{R}^n\}$ is joint articulated torque; and $F_{ex,i}\{(F_{w,i}^T, T_{w,i}^T)^T\}$ denote external forces/torque acting on the wheel [27]. More detailed simulation framework

**TABLE 3.** **Multi-Body dynamics simulation procedure.**

| | Algorithm 1: Multi-body dynamics simulation based on wheel–terrain interaction model |
|---|---|
| 1: | Input the digital elevation model map, normal surface vector for terrain inclination, terrain properties, rover geometry, mass, inertias, wheel parameters, normal load, and angular velocities on each wheel. |
| 2: | Set the initial state to be used in the first iteration. |
| 3: | Update the rover's vertical load considering the terrain inclination, position, orientation, and slip ratio with the derived dynamic states from the last iteration. |
| 4: | Calculate the forces and torque acting on each wheel based on the wheel–complex terrain interaction model. |
| 5: | Obtain the forces and torques acting on the system as outputs. |
| 6: | Solve the forward dynamics equation and then obtain the rover's positions, orientations, and velocities. |
| 7: | Calculate the tractive coefficient according to the rover's kinematic states. Return to Step 3 and iterate. |

and model are discussed in detail in the authors' previous publication [28].

## B. LOAD DISTRIBUTION WHEN ASCENDING INCLINED TERRAIN

In this subsection, the numerical analysis on the effect of body rotation in ascending deformable inclined terrain is presented. When the wheeled robot ascends an inclined deformable terrain, slippage can gradually accelerate with increasing inclination angle. That is, with the slippage behavior, the normal force on the downhill wheel side increases with the slope angle. In this situation, ascent may not progress or mobility performance may be degraded. A similar terrainability problem emerged when a previously designed and tested wheeled robot was deeply stuck on the terrain. In addition, the wheel torque, which is considerably, affected by the normal force, is the dominant factor influencing the available torque margin (called torque limitation).

The mechanical model of the robot's body pitching $\theta_p$ as the robot ascends the inclined deformable terrain is shown in Fig. 6. In this figure, $\alpha$ denotes the inclined surface angle, and $F_{UW}$ and $F_{DW}$ are the normal loads acting on the uphill and downhill wheel sides, respectively. These are expressed as follows.

$$F_{UW} = \frac{W}{2} - \frac{W}{L}\left(H \tan(\alpha) + A\frac{\sin(\alpha - \theta_p)}{\cos(\alpha)}\right), \quad (13)$$

$$F_{DW} = \frac{W}{2} + \frac{W}{L}\left(H \tan(\alpha) + A\frac{\sin(\alpha - \theta_p)}{\cos(\alpha)}\right). \quad (14)$$

Based on (13) and (14), the load becomes concentrated on the downhill wheel side when the robot leans along the slope. The wheel load distribution can be controlled by the pitch rotation of the body, as shown in Fig. 7. At this point, this compensation strategy is expected to transmit the normal force from the downhill to the uphill wheel side; this leads to
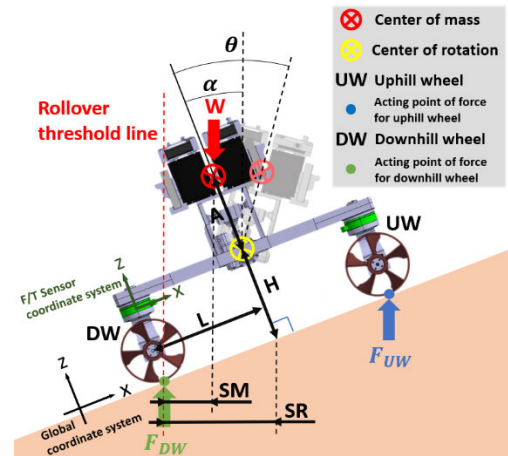


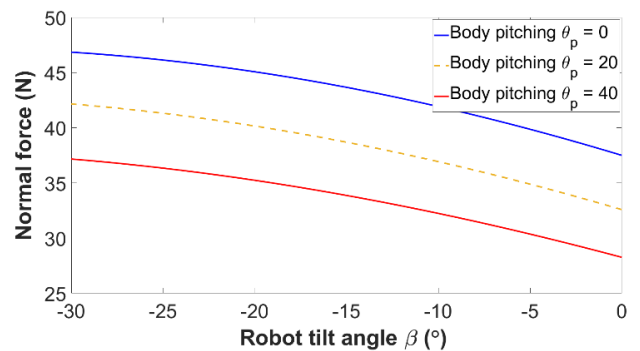**FIGURE 6.** Mechanical model for body pitching in forward slope.



**FIGURE 7.** Normal force of rear wheel according to body rotation while ascending inclined deformable terrain. Pitching center of mass diminishes normal force on downhill wheel side, suppressing slippage on deformable slope.

the suppression of the load concentration. If the body tilts or leans along the slope, rollover can be prevented by shifting the position of the robot's center of mass upward along the threshold line. As the robot ascends the inclined deformable terrain, the torque variation in the downhill wheel side according to the body rotation angle is shown in Fig. 8. The torque on the downhill wheel side increases with increasing slope angle
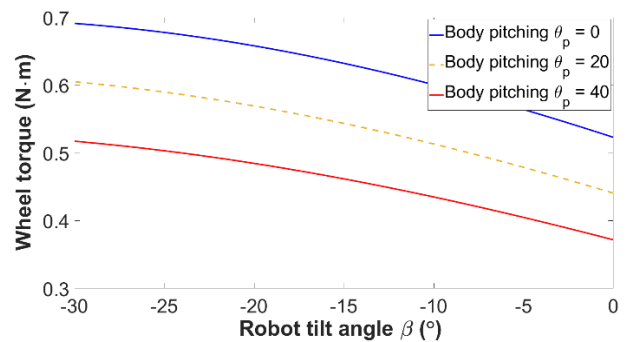


**FIGURE 8.** Rear wheel torque according to body pitching while ascending inclined deformable terrain. Pitching center of mass to positive direction decreases wheel torque on downhill side due to decreased normal force.

due to the increased normal force. As shown in Figs. 7 and 8, the normal force transmitted from the downhill to the uphill wheel side is expected to reduce the torque limitation criterion because of the increase in the available torque margin. At this point, equally dividing the normal force can improve the torque limitation with respect to the reduced wheel torque as the robot ascends the inclined deformable terrain.

### C. REDUCTION IN REQUIRED FRICTION COEFFICIENT WHEN SURMOUNTING BUMPY OBSTACLE

This subsection presents the numerical analysis that has been conducted to analyze the effect of body rotation on surmounting a rocky obstacle on a complex terrain. When the robot moving on level soil encounters a rocky obstacle and attempts to surmount it, the axle load and center of mass are shifted to the rear wheel side. Because the front wheel is lifted, the normal force on the front wheel decreases; as a result, the normal force on the rear wheel side increases; increasing the normal stress under the driving surface acting on the rear wheel may contribute to the collapse of the terrain.

The mechanical model of the robot's body pitching as it surmounts the rocky obstacle is shown Fig. 9. Here, $\theta_p$ is the pitch angle of the main body revolving around the center of rotation point; $\beta$ denotes the robot tilt angle with respect to the terrain inclination; $W$ represents the robot's mass; $F_{Z_{RW}}$ is the normal force acting on the rear wheel contact surface considering the terrain inclination; $F_{\mu_{RW}}$ is the required friction force affected by the normal force acting on the rear wheel side.
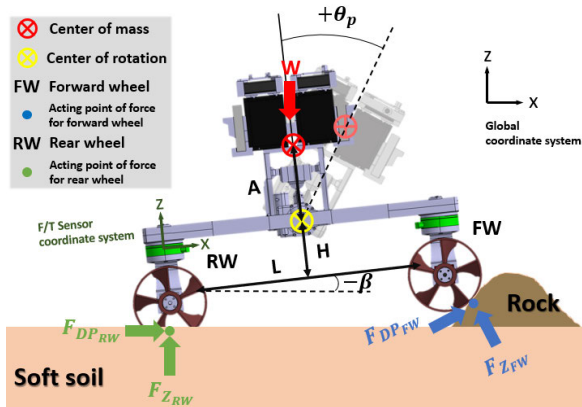


**FIGURE 9.** Mechanical model of body pitching as robot surmounts rocky obstacle.

The required friction coefficient, $\mu$, which is associated with the tractive coefficient under the rear wheel on the driving surface can be established from the normal and tangential forces when the robot leans along the terrain inclination. Using the multi-body dynamics simulation-based approach, the required friction coefficient is
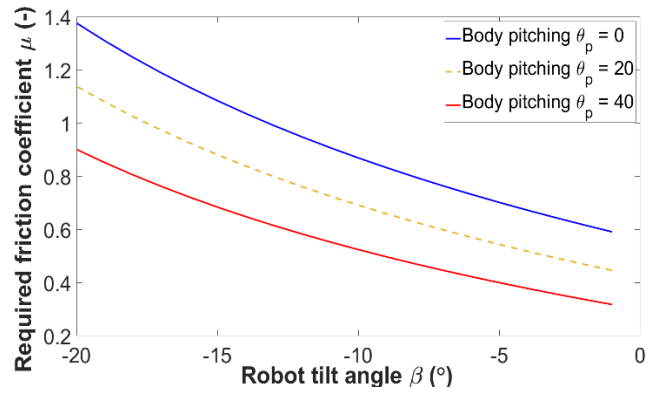
$$\mu = \frac{F_{DP}}{F_z}. \tag{15}$$



**FIGURE 10.** Required friction coefficient at rear wheel side to surmount rocky obstacle by body pitching. Pitching center of mass to positive rotation direction reduces normal force acting on rear wheel side and required friction coefficient for climbing.

Up to this point, the required friction coefficient is calculated according to various body rotations as the robot surmounts the bumpy obstacle, as shown in Fig. 10. The required friction force for the rear wheel decreases while the robot's body rotates to the positive direction. Because the normal force acting on the rear wheel is decreased with smaller wheel sinkage, the required friction coefficient also decreases. As can be seen, if the robot's body swivels from the negative direction to the positive direction, the robot can smoothly

surmount the obstacle. Note that this behavior is no need for more higher traction force beneath the rear wheel driving surface because of the lower required friction coefficient condition with smaller sinkage. At this point, reducing the required friction coefficient can enhance the trafficability related to the tractive coefficient for surmounting the bumpy obstacle.

### IV. OPTIMAL CONTROL STRATEGY AND NUMERICAL ANALYSIS FOR BODY ROTATION MECHANISM
#### A. BODY ROTATION ANGLE OPTIMIZATION
Prior to the conduct of the experimental verification, the optimal control problem is solved with the non–dominated sorting generic algorithm-II (NSGA-II), which uses an elitist principle and explicit diversity preserving mechanism. The algorithm is chosen because of its simplicity, high efficiency, excellent diversity–preserving mechanism, and fast convergence. The main parameters of NSGA-II include population ($N$), number of generations, crossover probability, mutation probability, crossover distribution index, and mutation distribution index. In the current optimization, the population size is set to 50, and 10 generations are formulated. Moreover, the probabilities for crossover and mutation are 0.9 and 0.04, respectively, whereas the distribution indexes for crossover and mutation are 25 and 25, respectively.

Fig. 11 shows the overall optimization procedure of body rotation configuration. Optimization procedures for coupling the robot dynamics model based on the wheel–complex
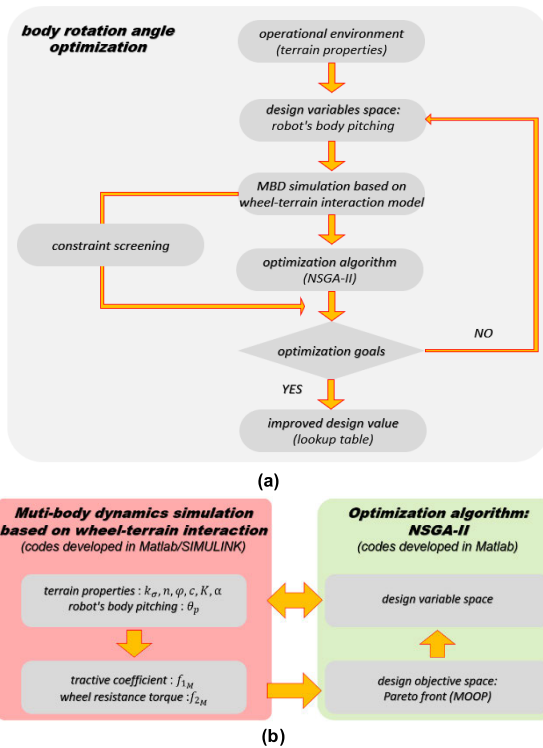
| Parameter (unit) | Value | |
|---|---|---|
| | Soft soil | Rock |
| *pressure sinkage modulus* $k_\sigma$ $(N/m^n)$ | 1594800 | 82000000 |
| *terrain deformation exponent* $n$ $(-)$ | 0.79 | 1 |
| *internal friction angle* $\varphi$ $(°)$ | 38.1 | 38.1 |
| *cohesion* $c$ $(Pa)$ | 460 | 0 |
| *fitted shear deformation modulus* $K$ $(m)$ | 0.01732 | 0.01732 |



**FIGURE 11.** Overall configuration of the multi-objective optimization procedure: (a) framework of the optimization procedure for optimal body rotation angle; (b) data flow for realization of optimization method.

terrain interaction and optimization algorithm are developed. The main problem of determining the necessary body pitching configuration that influences the tractive coefficient (related to trafficability) and wheel resistance torque (related to torque limitation) is solved in the dynamic state as the robot surmounts the bumpy obstacle and traverses the inclined deformable terrain. In solving the optimization problem, the operational environment conditions are considered according to the rocky obstacle ranging in height from 0.1 to 0.25 m, and the deformable terrain inclined within the angle range 10°–30°. Moreover, the body rotation angles gradually change from −60° to 60°. Table 4 summarizes the other parameters related to the terrain parameter [29]. The objective functions for tractive coefficient, $f_{1_M}$, and wheel resistance torque, $f_{2_M}$, are defined as

$$\textbf{\textit{Find }} d \in R^n, \quad d = \{d_1 : \theta_p\} \textbf{ \textit{that}}$$
$$f_{1_M}(d_1) = min(-F_{DP}/F_z)$$
$$f_{2_M}(d_1) = min(T_w). \quad (16)$$

The details of the multi–objective optimization procedure combined with the robot dynamics model and NSGA-II are as follows. First, the main parameters of NSGA-II, robot dynamics model, and initial parameter design values, which are shared with the design parameter space of the optimization process, are inputted. Second, the tractive coefficient and wheel resistance torque are solved using the robot dynamics model based on the wheel–complex terrain interaction;

the results are forwarded to the design objective space of the optimization process. Third, the optimization algorithm determines the design parameter for the next group that are to be used for the generation and feedback of the robot dynamics model. This process set is actuated by the optimization algorithm and does not stop until the preset generation number is completed. Finally, the derived optimal body rotation angles and terrain inclinations are gathered and recorded. These data are arranged into matrix form for the lookup table.

### B. VERIFICATION OF OPTIMIZATION FOR BODY ROTATION CONTROL SCHEME

#### 1) MULTI–BODY DYNAMICS SIMULATION: SIMULATION ENVIRONMENT
Prior to the conduct of the experimental verification, the multi-body dynamics simulation is performed based on the wheel–complex terrain interaction with the proposed mechanism. This result shows the effectiveness of optimization results and the proposed body rotation mechanism. For the multi-body dynamics simulation, the scenarios considered include the rocky obstacle and inclined deformable terrain as controlled and uncontrolled, as shown in Figs. 12 and 13. These driving environments are generated by a digital elevation map, which merges the terrain elevation coordinates and terrain properties data as soft soil and/or rocky terrain.
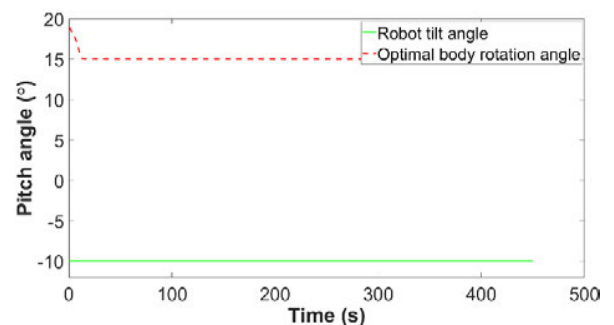


**FIGURE 12.** Time profile of wheeled robot's tilt angle with respect to terrain inclination and derived optimal body control configuration for ascending 10° deformable inclined terrain.

#### 2) MULTI–BODY DYNAMICS SIMULATION: ASCENDING 10° INCLINED DEFORMABLE TERRAIN
This subsection presents the multi-body dynamics simulation results from the sample case study to analyze the effect of
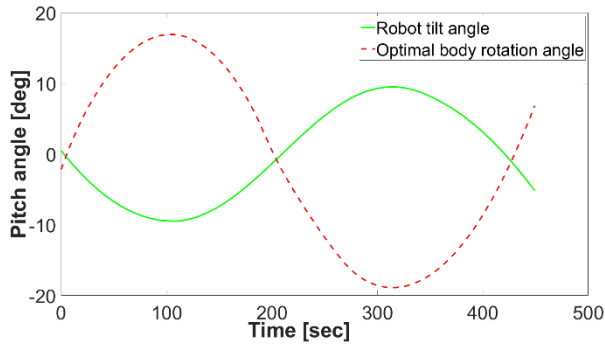
**FIGURE 13.** Time profile of wheeled robot's tilt angle with respect to the terrain inclination and derived optimal body control configuration for surmounting rocky obstacle more than 0.1 m high with level soft soil.

optimal body rotation control strategies as the robot ascends a 10° slope with soft soil. The terrain inclination and derived optimal pitch angle as control command are shown in Fig. 12.

The simulation results for the relationship between time and normal force, drawbar pull, wheel torque, and tractive coefficient (related to trafficability) according to the controlled and uncontrolled body rotation when the robot is on the inclined soft soil surface are shown Figs. 14–17. In the uncontrolled body rotation case, when the robot ascends the inclined slope with soft soil, the normal force and wheel
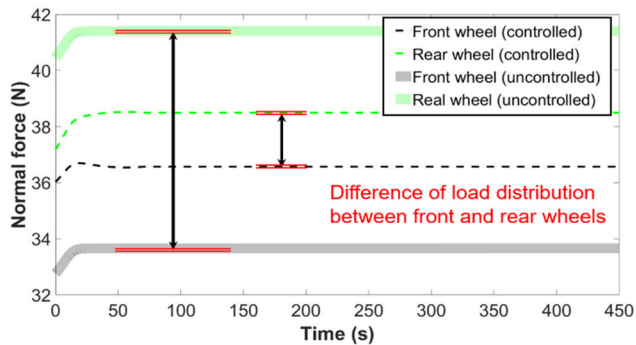


**FIGURE 14.** Simulation result: normal forces acting on front and rear wheels (controlled and uncontrolled conditions). By shifting center of mass based on optimal control strategy, difference of load distribution between front and rear wheels become smaller.
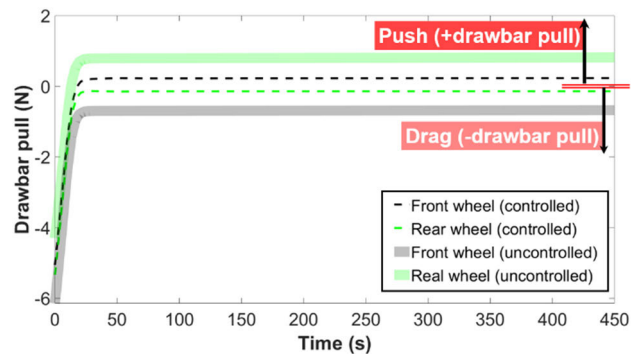


**FIGURE 15.** Simulation result: drawbar pull acting on front and rear wheels (controlled/uncontrolled condition).
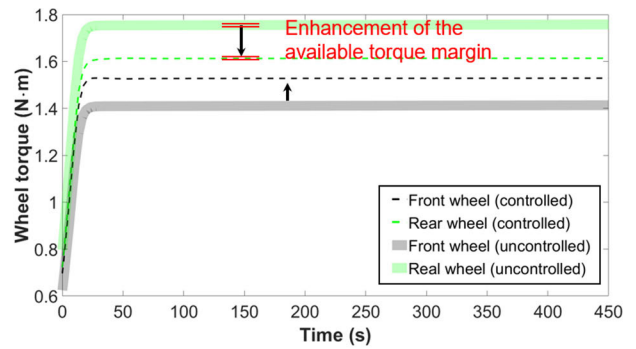


**FIGURE 16.** Simulation result: wheel torque acting on front and rear wheels (controlled and uncontrolled conditions). The shift of the center of mass can be helpful for the +8% enhancement of available torque margin.
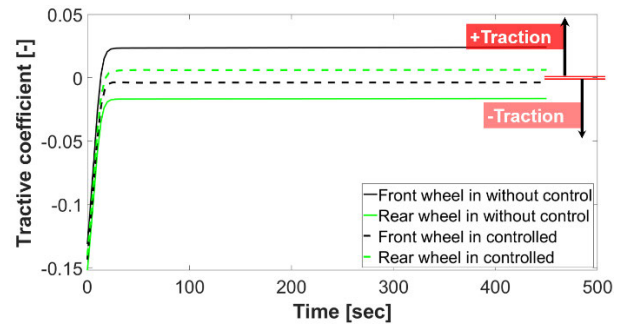


**FIGURE 17.** Simulation result: tractive coefficient on front and rear wheels (controlled and uncontrolled conditions).

torque on the downhill wheel side exceed those on the uphill wheel side. In addition, as shown in Fig. 14, if the driving motors on the downhill wheel side were stopped due to the pre-defined torque limitation, the wheel torque on the uphill wheel side becomes concentrated. In this situation, climbing may not progress, or the torque limit of all driving motors may be exceeded, leading to malfunction.

As depicted in Figs. 14–17, in the controlled case, the normal force, drawbar pull, wheel torque, and tractive coefficient become almost equal by shifting the center of mass via the derived optimal pitch control command. In particular, as shown in Fig. 16, the rear wheel torque in the controlled case is less than that in the uncontrolled case. The shift in the center of mass contributes to the +8% torque margin with respect to the reduced wheel torque. At this point, this compensation strategy equally divides the normal force by shifting the center of mass via the preferred optimal body pitch configuration. It is expected to effectively suppress the load concentration and enhance the mobility limit in accordance with the torque limitation.

### 3) MULTI–BODY DYNAMICS SIMULATION: SURMOUNTING 0.1-m ROCKY OBSTACLE ON SOFT SOIL

The multi–body dynamics simulation is also conducted to analyze the effect of optimal body rotation control strategies when the robot surmounts a 0.1-m rocky obstacle on soft soil.

This case involves surmounting rocky obstacle in three sections: soft soil, hard rocky obstacle, and soft soil. The terrain inclination with respect to the hard rock and derived optimal pitch angle as control command are shown in Fig. 13.

The simulation results of the relationship between time and normal force, drawbar pull, wheel torque, and tractive coefficient according to the controlled/uncontrolled body rotation given a 0.1-m high rocky obstacle on soft soil are shown in Figs. 18–21. In the uncontrolled body rotation case, the
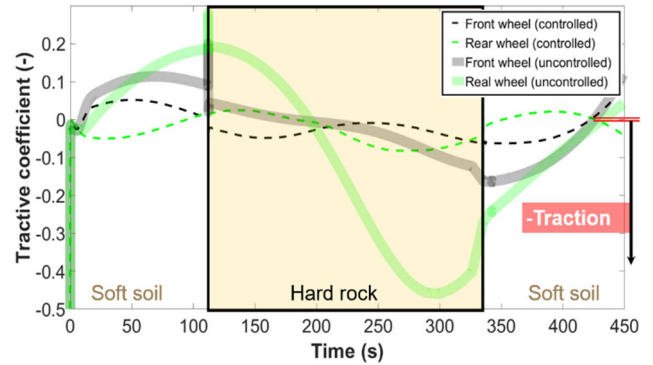


**FIGURE 18.** Simulation result: normal forces acting on front and rear wheels (controlled and uncontrolled conditions).



**FIGURE 19.** Simulation result: drawbar pull acting on front and rear wheels (controlled and uncontrolled conditions).



**FIGURE 20.** Simulation result: wheel torque acting on front and rear wheels (controlled and uncontrolled conditions). While facing rocky obstacle the wheel torque in uncontrolled case is larger than the wheel torque in controlled condition.



**FIGURE 21.** Simulation result: tractive coefficient on front and rear wheels (controlled and uncontrolled conditions). The shift of center of mass can be helpful for the +82% improvement of mobility performance as negative value of tractive coefficient is diminished.

normal force is drastically shifted to the rear wheel side when the wheel comes into contact with the rocky obstacle, as shown in Fig. 18. Because the front wheel is lifted when the robot moves from the flat soil surface toward the rocky obstacle, the normal force on the front wheel side is decreased. As a result, as shown in Figs. 19 and 20, the drawbar pull and wheel torque considerably increase as the robot surmounts the hard rock. However, after contact with the rock, the normal force is observed to shift between the front and rear wheels. The drawbar pull and torque also decrease; this may be caused by the sudden decrease in the robot's velocity. The drawbar pull and wheel torque have negative values because of the wheel drag resulting from slippage. Furthermore, this phenomenon considerably reduces tractive coefficient, as shown in Fig. 21. In particular, the tractive coefficient of the rear wheel side has a negative value because of the lack of traction.

As shown in Figs. 18–21, in the controlled case, shifting the center of mass via the derived optimal pitch control command, normal force, drawbar pull, wheel torque, and tractive coefficient become almost equal. In particular, if the drawbar pull and torque have positive values and/or approach zero, the full magnitudes of the force and torque are delivered without substantial power loss to the robot's dynamic behavior. In addition, the drawbar pull and torque of the rear wheel are less than that in the uncontrolled case. In particular, the shift in the center of mass contributes to the +82% enhancement of mobility performance with respect to the reduced negative value of tractive coefficient. Note that this behavior is not required for achieving a higher traction force to overcome the rocky obstacle. If the robot's body appropriately swivels, the safety and gradeability of the robot can be enhanced with less electricity consumption (which is affected by the wheel torque). With lower wheel slippage, trafficability (which is affected by the tractive coefficient) is higher due to the uniform load distribution. Consequently, the robot smoothly bumps and surmounts the rocky obstacle.
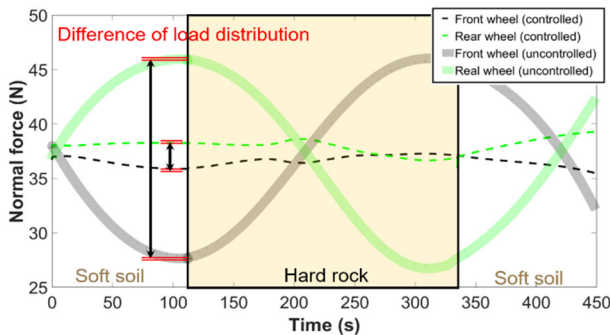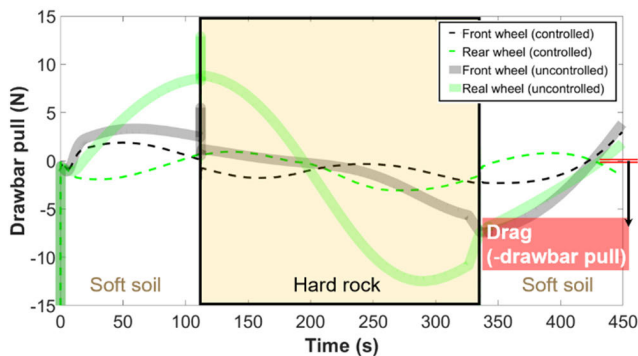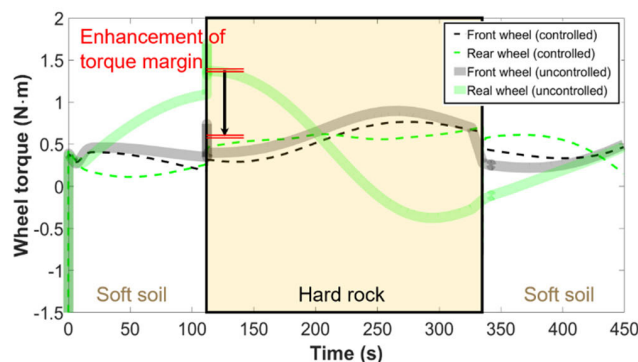
## V. FIELD TEST FOR MOBILITY PERFORMANCE EVALUATION

### A. SLOPE-CLIMBING FIELD TEST

#### 1) EXPERIMENTAL SETUP

A robot platform, which can be controlled for the robot's body pitch angle, was manufactured based on the theoretical and numerical analysis results. An outdoor experiment was performed to test the actual performance and effectiveness of the body rotation mechanism. As previously mentioned, this system comprises the wheel encoder sensor with the motor, current sensor, inclinometer, and force/torque sensor. In this setup, each wheel is controlled to drive with a constant angular velocity of 0.0625 rad/s by the PID control. The experimental scene for surmounting the rocky/bumpy obstacle and traversing the inclined soft soil is shown in Fig. 22. The field tests consists of two parts with two patterns: controlled and uncontrolled body rotation control. In the former case, the pitch angle of the robot's body is changed according to the preferred angle listed in the lookup table data for the optimal pitch configuration with respect to the terrain inclination, as shown in Figs. 23 and 24. After multiple experiments, the average values of the normal force, drawbar pull, wheel torque, tractive coefficient, terrain inclination, and body pitch angle are calculated.



**FIGURE 22.** Field test operational environment on (a) terrain approximately inclined at 17° and (b) 0.22-m rocky obstacle under soft soil.
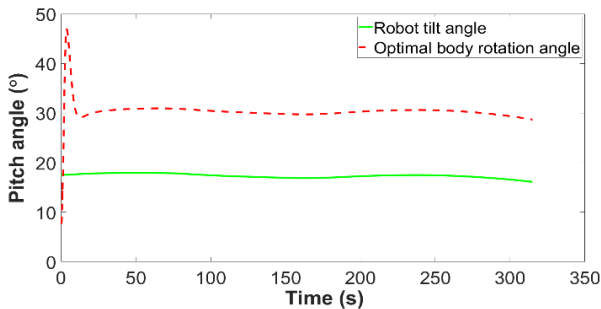


**FIGURE 23.** Field test result: time profile of wheeled robot's tilt angle with respect to terrain inclination and derived optimal body control configuration for climbing deformable terrain inclined at approximately 17°.

#### 2) RESULT OF SLOPE-CLIMBING FIELD TEST

Slope-climbing field tests were also performed to confirm the actual mobility performance related to improving the load concentration and torque limitation according to the controlled/uncontrolled body rotation as the robot ascends a
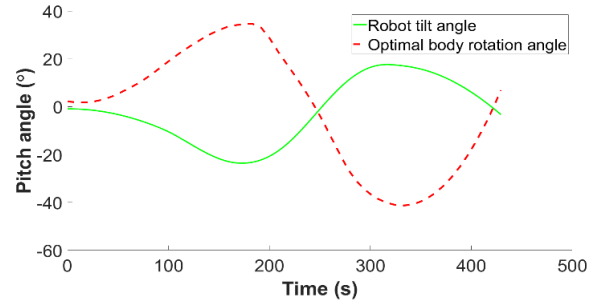


**FIGURE 24.** Field test result: time profile of wheeled robot's tilt angle with respect to terrain inclination and derived optimal body control configuration for surmounting 0.22-m rocky obstacle.

slope with soft soil inclined at approximately 17°. The terrain inclination and control command regarding the optimal body rotation control strategy is shown in Fig. 23.

The results in Figs. 25–28 show that the normal force, drawbar pull, wheel torque, and tractive coefficient when the robot movement is on the downhill side exceed those when the robot is on the uphill side because of the load concentration in the uncontrolled case. In the same case, the drawbar pull on the uphill wheel side is approximately $(-9.2)$–$(-0.5)$, as shown in Fig. 26. Because the normal
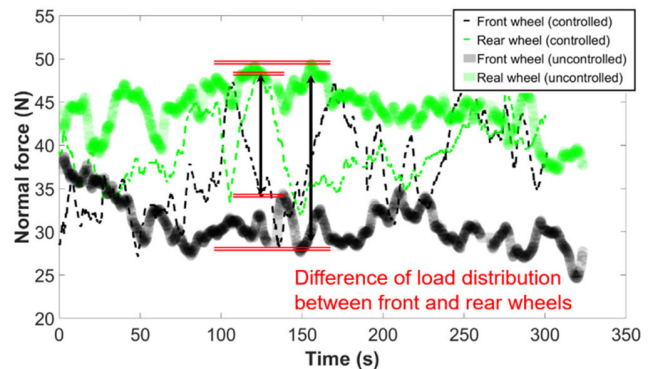


**FIGURE 25.** Field test result: normal force acting on front and rear wheels (controlled and uncontrolled conditions). Normal force is equally divided by shifting center of mass based on optimal control strategy.
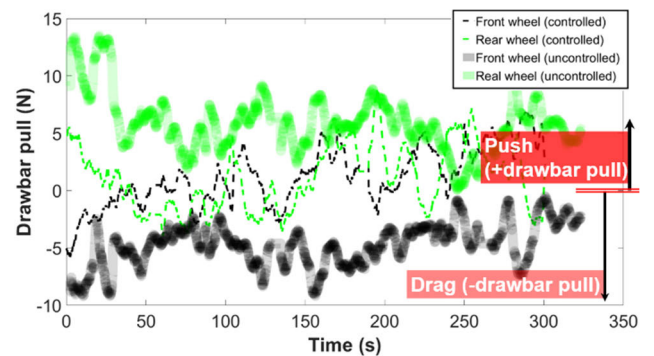


**FIGURE 26.** Field test result: drawbar pull acting on front and rear wheels (controlled and uncontrolled conditions).
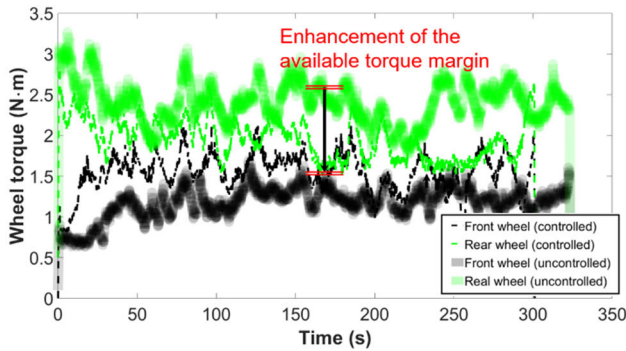
**FIGURE 27.** Field test result: wheel torque acting on front and rear wheels (controlled and uncontrolled conditions). Shift in center of mass slightly contributes to enhancement of available torque margin due to equally divided normal force.
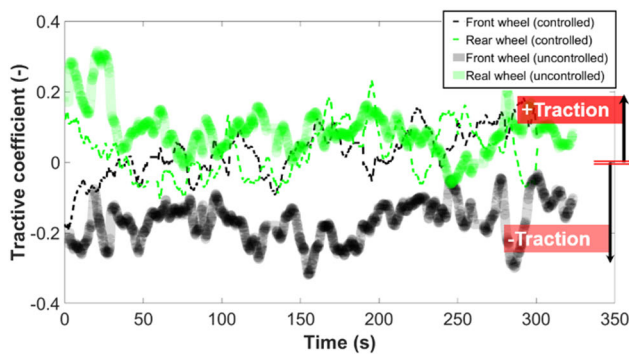


**FIGURE 28.** Field test result: tractive coefficient on front and rear wheels (controlled and uncontrolled conditions).

force acting on the uphill wheel side decreased, the resistance force from the uphill wheel side should be delivered to the robot's body due to effect of the negative drawbar pull; consequently, mobility performance may be downgraded. Moreover, the tractive coefficient on the uphill side has a negative value because of the lack of traction, as depicted in Fig. 28. The load distribution in the controlled case can be effectively regulated based on the optimal body rotation control strategy. In this situation, the differences in the drawbar pull, wheel torque, and tractive coefficient between the uphill and downhill wheels are smaller in the controlled case. In particular, the maximum wheel torque was reduced compared with that in the uncontrolled case. The minimum wheel torque in the controlled case is −42.8% relative to that of the uncontrolled case (2.658 N·m → 1.52 N·m). This conclusion is consistent with the robot dynamic simulation results. This implies that proposed body rotation mechanism with appropriate body pitch configuration is an effective approach to solve the load concentration and torque limitation problems, when the robot ascends inclined deformable terrain.

### B. BUMPY OBSTACLE PASSING FIELD TEST AND DISCUSSION
#### 1) RESULT OF BUMPY OBSTACLE FIELD TEST
Field tests were conducted to verify the actual mobility performance and effectiveness of the body rotation control

strategy while overcoming the rocky obstacle on soft soil. In the bumpy obstacle field test, the height of the rocky obstacle on the deformable terrain is approximately 0.22-m. The terrain inclination relative to the hard rock and control command pertaining to the robot's body pitch angle is shown in Fig. 24.

In the case of the uncontrolled body rotation, the normal force on the rear wheel side exceeds that on the front wheel when coming into contact with the rocky obstacle, as shown in Fig. 29. In contrast, the difference of the load distribution between the front and rear wheel becomes small when the center of mass is shifted via the optimal pitch control strategy. Because of this, in Fig. 30, the difference in the drawbar pull between the front and rear wheel sides considerably decreases compared with that in the uncontrolled body rotation control case. Moreover, the maximum wheel torque in the controlled case is −38.6% relative to that in the uncontrolled case (3.708 Nm → 2.28 Nm). Thus, when the robot's body appropriately swivels, the wheel torque margin slightly increases, as shown in Fig. 31. In the controlled case, the minimum tractive coefficient related to trafficability is +87.5% relative to that in the uncontrolled case (−1.2 → −0.15) as shown in Fig. 32. Note that the proposed body rotation mechanism with the optimal control strategy can considerably enhance trafficability (affected by tractive coefficient) with improved torque margin. Consequently, the robot can also smoothly surmount the rocky obstacle on the deformable terrain using less electricity.
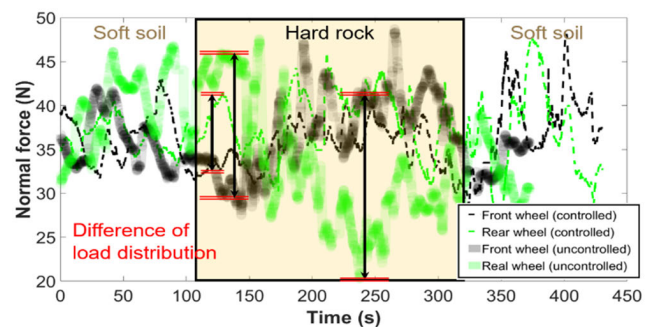


**FIGURE 29.** Field test result: normal force acting on front and rear wheels (controlled and uncontrolled conditions). Difference in normal force in uncontrolled case is also larger than that in controlled case.

#### 2) DISCUSSION
This study presents a reconfigured robot system, which facilitates changes in the rover internal force and torques by applying body rotation with an appropriate configuration strategy. In addition, dynamic optimization procedure integrating a robot dynamic model based on the wheel-complex terrain interaction and NSGA-II was developed to determine the optimal body rotation configuration. In particular, the effectiveness of this mechanism was demonstrated in the robot dynamics analysis and experiments. The specific operational environment that was considered to experimentally validate the enhanced mobility performance related to the
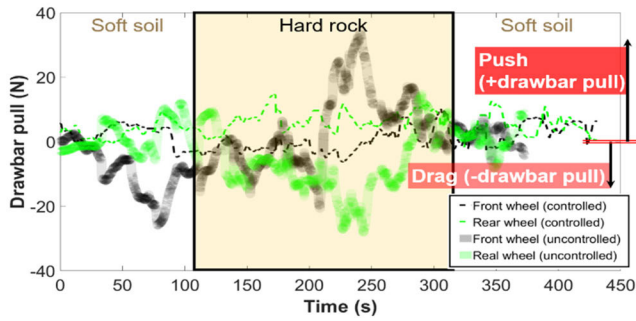
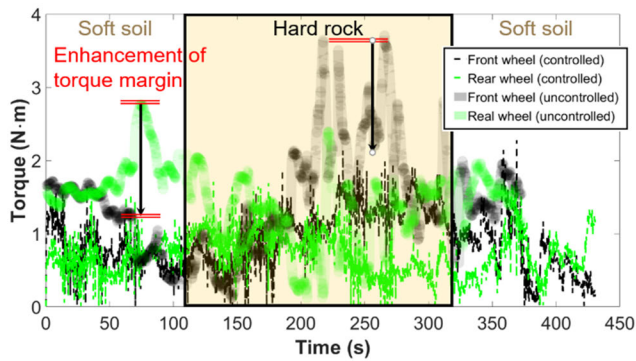**FIGURE 30.** Field test result: drawbar pull acting on front and rear wheels controlled/uncontrolled.



**FIGURE 31.** Field test result: wheel torque acting on front and rear wheels (controlled and uncontrolled conditions).
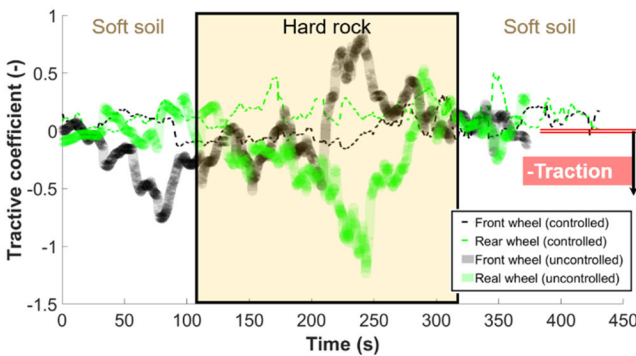


**FIGURE 32.** Field test result: tractive coefficient on front and rear wheels (controlled/uncontrolled). Negative effect of mobility performance can be improved if negative value of tractive coefficient is diminished by shifting center of mass to positive direction.

trafficability with lower electricity involves load distribution and torque limitation. From a realistic perspective, this operational environment is associated with the complex deformable terrain. Both numerical analysis and field test under the given operational environment demonstrated the effectiveness of the proposed mechanism by readjusting the pitch angle of the robot. Moreover, using the internal gyro-accelerometer sensor, the proposed mechanism can realize its body attitude with respect to the terrain inclination. Thus, this ensures proper controlled body roll angle as well as pitch angle with respect to more extremely side inclined/downward

ground, even though it is not highlighted in this report. Hence, the mechanism may be adjusted to any ground inclination as necessary. To investigate the limitation of the maneuvering capabilities realistically, a traversability assessment standard for the body rotation control strategy is required.

Moreover, recent meteorite search on the Antarctic/lunar prospector mission found evidence of an excellent medium for the detection of high-energy neutrinos and volatiles for the water ice on lunar surface. In this region, the wheeled robot used in solar power generally suffers lack of power condition due to the low angles of sunlight. Thus, if it follows the solar position to clock sunlight, this enables unprecedented range of the operation with advantages to survivability and persistent power. Thus, we discuss here the additional side effect for enhanced solar irradiation related to the power acquisition to provide some guideline for energy requirement in the future exploration missions. For solar irradiation, we have assumed a solar cell efficiency of $\eta_{cell} = 27\%$, which is the maximum solar cell efficiency commercially obtained nowadays under a best-case scenario, and a solar panel area of 1-$m^2$. In Fig. 33 and Table 5, numerical analysis for solar irradiation show that effectiveness of the pointable solar panel by following a spiraling path by proposed mechanism in order to maintain Sun-synchronous. In particular, if the solar array is fixed, total amount of solar irradiation remarkably decreases as the latitude increases rather than obtained by body rotation mechanism. To safely operate Sun-synchronous, we consider the relevant operation range of panel orientation with the limit of 7° in rotation angle, in order to prevent chassis damage and immobilization of robot. Meanwhile, more reliable numerical/experimental verification for these side effects are



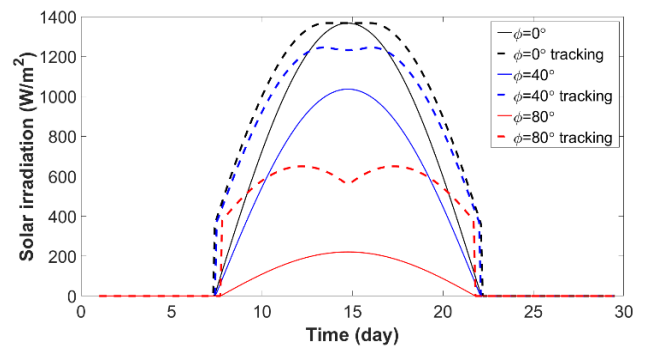**FIGURE 33.** Solar irradiation according to various latitude region on the Moon in the case of the fixed flat surface and pointable solar panel via body rotation mechanism.

**TABLE 5.** Results of estimated solar irradiation by pointable solar panel by proposed mechanism according to latitude.

| Latitude Ø | Additional acquired solar irradiation |
|---|---|
| Ø = 0° | 22.9% |
| Ø = 40° | 48.8% |
| Ø = 80° | 306.3% |

required, which will be investigated further in future studies. However, these are beyond the scope of this paper.

All these supplementary considerations will be included in our future study. Despite these limitations, the proposed reconfiguration of the robot system has considerable potential in traversing complex terrains. The mobility performance of this robot can be enhanced by reducing the wheel torque related to the torque limitation criterion and suppressing the load concentration. This can increase the tractive coefficient compared with that in the uncontrolled fixed body configuration.

## VI. CONCLUSION

This research proposed a wheeled robot platform with body rotation mechanism and its optimal control configuration integrated to the robot dynamics model and NSGA-II.

The major accomplishments of this research are summarized as follows.

1) A wheeled robot platform with a body rotation mechanism was designed and fabricated to enhance the mobility performance for surmounting rocky obstacles and traversing soft soil slopes.
2) The mechanical model and robot dynamics model based on the wheel–complex terrain interaction were described to verify the effectiveness of the proposed mechanism.
3) Optimal body rotation configurations, which considered both tractive coefficient and wheel torque, were obtained by the developed robot dynamics model and NSGA-II considering various dynamic states.
4) Based on the numerical analysis results, the field test for surmounting the bumpy obstacle and travel on the deformable slope were conducted according to the controlled/uncontrolled condition.

These results demonstrated that the proposed robot platform with the body rotation mechanism reduced the load concentration and the required traction force (related to the tractive coefficient) for climbing hard rock. In the case of traversing an inclined terrain, the controlled load distribution enhanced the torque limitation beyond that in the uncontrolled case. Based on these results, the proposed body rotation mechanism proposed in this work is deemed an effective approach for enhancing the mobility performance of a robot on a complex terrain.

## REFERENCES

[1] M. Sutoh, J. Yusa, T. Ito, K. Nagatani, and K. Yoshida, "Traveling performance evaluation of planetary rovers on loose soil," *J. Field Robot.*, vol. 29, no. 4, pp. 648–662, Jul. 2012.

[2] K.-J. Kim, S.-H. Kim, and K.-H. Yu, "Design of a wheel test bed for a planetary exploration and driving experiment," *J. Inst. Control, Robot. Syst.*, vol. 21, no. 4, pp. 372–377, Apr. 2015.

[3] B. Ghotbi, F. González, J. Kövecses, and J. Angeles, "Vehicle-terrain interaction models for analysis and performance evaluation of wheeled rovers," in *Proc. IEEE/RSJ Int. Conf. Intell. Robots Syst.*, Oct. 2012, pp. 3138–3143.

[4] B. Ghotbi, F. González, J. Kövecses, and J. Angeles, "Mobility assessment of wheeled robots operating on soft terrain," in *Field and Service Robotics*. Cham, Switzerland: Springer, 2016, pp. 331–344.

[5] Y. Chang, D. Tan, H. Wang, and S. Ma, "Kinematics analysis of a six-wheeled mobile robot," in *Proc. IEEE/RSJ Int. Conf. Intell. Robots Syst.*, Oct. 2006, pp. 4169–4174.

[6] Y. Kuroda, K. Kondo, K. Nakamura, Y. Kunii, and T. Kubota, "Low power mobility system for micro planetary rover micro 5," in *Proc. Artif. Intell., Robot. Automat. Space*, vol. 440, 1999, pp. 77–82.

[7] Y. Bai, L. Sun, and M. Zhang, "Terramechanics modeling and grouser optimization for multistage adaptive lateral deformation tracked robot," *IEEE Access*, vol. 8, pp. 171387–171396, 2020.

[8] D. Apostolopoulos, "Analytical configuration of wheeled robotic locomotion," Robot. Inst., Carnegie Mellon Univ., Pittsburgh, PA, USA, Tech. Rep. CMU-RI-TR-01-08, 2001.

[9] T. Thüer, "Mobility evaluation of wheeled all-terrain robots: Metrics and application," Ph.D. dissertation, Dept. Mech. Process Eng., ETH Zürich, Zürich, Switzerland, 2009.

[10] Y. Shen, G. Zhang, Y. Tian, and S. Ma, "Development of a wheel-paddle integrated quadruped robot for rough terrain and its verification on hybrid mode," *IEEE Robot. Autom. Lett.*, vol. 3, no. 4, pp. 4062–4067, Oct. 2018.

[11] W. Wang, H. Xu, X. Xu, and F. Zhou, "Enhancing the passing ability of unmanned vehicles using a variable-wheelbase driving system," *IEEE Access*, vol. 7, pp. 115871–115885, 2019.

[12] L. Yang, B. Cai, R. Zhang, K. Li, Z. Zhang, J. Lei, B. Chen, and R. Wang, "Mechanical analysis and performance optimization for the lunar rover's vane-telescopic walking wheel," *Engineering*, vol. 6, no. 8, pp. 936–943, Aug. 2020.

[13] T. Kislassi and D. Zarrouk, "A minimally actuated reconfigurable continuous track robot," *IEEE Robot. Autom. Lett.*, vol. 5, no. 2, pp. 652–659, Apr. 2020.

[14] S. Kakkar and M. A. Minor, "Fast and reliable motion model for articulated wheeled mobile robots on extremely rough and rocky terrains," *IEEE Robot. Autom. Lett.*, vol. 4, no. 3, pp. 2252–2259, Jul. 2019.

[15] D. Fujiwara, T. Oshima, and K. Iizuka, "Measuring the normal stress distribution acting on a locked-wheel of push–pull locomotion rovers via a wheel sensor system," *Sensors*, vol. 20, no. 16, pp. 1–22, 2020.

[16] S. Nakamura, M. Faragalli, N. Mizukami, I. Nakatani, Y. Kunii, and T. Kubota, "Wheeled robot with movable center of mass for traversing over rough terrain," in *Proc. IEEE/RSJ Int. Conf. Intell. Robots Syst.*, San Diego, CA, USA, Oct. 2007, pp. 1228–1233.

[17] M. Yokoyama, Y. Matsuhasi, A. Sano, and M. T. Ko, "Slip control of a wheeled mobile robot with a movable auxiliary mass," in *Proc. IEEE Int. Conf. Adv. Intell. Mechatronics (AIM)*, Jul. 2015, pp. 1008–1013.

[18] M. Blodnick, "Planetary mission preplanning with heading-specific slope and distance from shadow," Robot. Inst., Carnegie Mellon Univ., Pittsburgh, PA, USA, Tech. Rep. CMU-RI-TR-17-23, Jun. 2017.

[19] F. Cordes, C. Oekermann, A. Babu, D. Kuehn, T. Stark, and F. Kirchner, "An active suspension system for a planetary rover," in *Proc. 12th Int. Symp. Artif. Intell., Robot. Automat. Space (i-Sairas)*, Montreal, QC, Canada, 2014, pp. 17–19.

[20] P. Sandin, *Robot Mechanisms and Mechanical Devices Illustrated*. New York, NY, USA: McGraw-Hill, 2003, p. 134.

[21] H. Inotsume, M. Sutoh, K. Nagaoka, K. Nagatani, and K. Yoshida, "Evaluation of the reconfiguration effects of planetary rovers on their lateral traversing of sandy slopes," in *Proc. IEEE Int. Conf. Robot. Autom.*, May 2012, pp. 3413–3418.

[22] G. Ishigami, "Terramechanics-based analysis and control for lunar/planetary exploration robots," Ph.D. dissertation, Dept. Aerospace Eng., Tohoku Univ., Sendai, Japan, 2008.

[23] E. Strickland and G. Zorpette, "The coming moon rush: Technology, billionaires, and geopolitics will all help get us back to the moon, but they won't be enough to let us live there indefinitely," *IEEE Spectr.*, vol. 56, no. 7, pp. 22–25, Jul. 2019.

[24] W. Whittaker, G. Kantor, B. Shamah, and D. Wettergreen, "Sun-synchronous planetary exploration," in *Proc. Space Conf. Expo.*, Sep. 2000, p. 5300.

[25] B.-S. Sim, K.-J. Kim, and K.-H. Yu, "Development of body rotational wheeled robot and its verification of effectiveness," in *Proc. IEEE ICRA*, May 2020, pp. 10405–10411.

[26] E. Talvila and M. Wiersma, "Simple derivation of basic quadrature formulas," 2012, *arXiv:1202.0249*. [Online]. Available: http://arxiv.org/abs/1202.0249

[27] K. Yoshida and B. Wilcox, "Space robots," in *Springer Handbook of Robotics*, B. Siciliano and O. Khatib, Eds. Springer, 2008, pp. 1031–1063.

[28] K.-J. Kim and K.-H. Yu, "Multidisciplinary design optimization for a solar-powered exploration rover considering the restricted power requirement," *Energies*, vol. 13, no. 24, pp. 1–28, 2020.

[29] H. Yang, L. Ding, H. Gao, L. Huang, J. Guo, C. Chen, and Z. Deng, "Dynamic simulation of planetary rovers with terrain property mapping," in *Proc. IEEE ICRA*, May 2018, pp. 738–743.

**BYEONG-SEOP SIM** received the B.S. and M.S. degrees in aerospace engineering from Jeonbuk National University, Jeonju, South Korea, in 2017 and 2019, respectively.

He is currently a Researcher with the Department of Production Engineering, UCONSYSTEM Company Ltd., Daejeon, South Korea. His research interests include the control system of UGV and machine design.

**KEE-HO YU** (Senior Member, IEEE) received the B.S. and M.S. degrees in mechanical engineering from Jeonbuk National University, Jeonju, South Korea, in 1988 and 1990, respectively, and the Ph.D. degree in mechanical engineering from Tohoku University, Sendai, Japan, in 1994.

From 1994 to 1997, he was a Research Associate with Tohoku University. He became a Lecturer with the Department of Aerospace Engineering, Jeonbuk National University, in 1998, where he has been a Professor, since 2009. From 2004 to 2005, he was a Visiting Professor with Massachusetts Institute of Technology. His research interests include the design of solar powered UAV, control/operation of drones, design of wheeled robots, and tactile display and its application.

Prof. Yu is a member of the Institute of Control, Robotics and Systems, the Korean Society for Aeronautical and Space Sciences, the Robotics Society of Japan, and the Society of Instrument and Control Engineers.

**KUN-JUNG KIM** received the B.S., M.S., and Ph.D. degrees in aerospace engineering from Jeonbuk National University, Jeonju, South Korea, in 2015, 2017, and 2020, respectively.

He is currently a Postdoctoral Researcher with the Aerospace Robotics and Mechatronics Laboratory, Jeonbuk National University. His current research interests include multi-body dynamics simulation based on the wheel–terrain interaction model and design and control of wheeled robot.

・・・